



1 **Mapping long-term and high-resolution global gridded photosynthetically active**
2 **radiation using the ISCCP H-series cloud product and reanalysis data**

3 Wenjun Tang¹, Jun Qin², Kun Yang³, Yaozhi Jiang³

4 1. National Tibetan Plateau Data Center (TPDC), State Key Laboratory of Tibetan
5 Plateau Earth System, Environment and Resources (TPESER), Institute of Tibetan
6 Plateau Research, Chinese Academy of Sciences, Beijing 100101, China.

7 2. State Key Laboratory of Resources and Environmental Information System, Institute
8 of Geographic Sciences and Natural Resources Research, Chinese Academy of
9 Sciences, Beijing 100101, China.

10 3. Department of Earth System Science, Ministry of Education Key Laboratory for
11 Earth System Modeling, Institute for Global Change Studies, Tsinghua University,
12 Beijing 100084, China.

13

14

15 Corresponding author and address:

16 Dr. Wenjun Tang

17 Institute of Tibetan Plateau Research, Chinese Academy of Sciences

18 Building 3, Courtyard 16, Lin Cui Road, Chaoyang District, Beijing 100101, China

19 Email: tangwj@itpcas.ac.cn

20 Tel: +86-10-84097046

21 Fax: +86-10-84097079



22 **Abstract:** Photosynthetically active radiation (PAR) is a fundamental physiological
23 variable for research in the ecological, agricultural, and global change fields. In this
24 study, we produced a 35-year (1984–2018) high-resolution (3 h, 10 km) global gridded
25 PAR dataset using an effective physical-based model. The main inputs of the model
26 were the latest International Satellite Cloud Climatology Project (ISCCP) H-series
27 cloud products, MERRA-2 aerosol data, ERA5 surface routine variables, and MODIS
28 and CLARRA-2 albedo products. Our gridded PAR product was evaluated against
29 surface observations measured at seven experimental stations of the SURFACE
30 RADIATION budget network (SURFRAD), 42 experimental stations of the National
31 Ecological Observatory Network (NEON), and 38 experimental stations of the Chinese
32 Ecosystem Research Network (CERN). Instantaneous PAR was validated against
33 SURFRAD and NEON data; mean bias errors (MBE) and root mean square errors
34 (RMSE) were, on average, 5.8 W m^{-2} and 44.9 W m^{-2} , respectively, and correlation
35 coefficient (R) was 0.94 at the 10 km scale. When upscaled to 30 km, the errors were
36 markedly reduced. Daily PAR was validated against SURFRAD, NEON, and CERN
37 data, and the RMSEs were 13.2 W m^{-2} , 13.1 W m^{-2} , and 19.6 W m^{-2} , respectively at the
38 10 km scale. The RMSEs were slightly reduced when upscaled to 30 km. Compared
39 with the well-known global satellite-based PAR product of the Earth's Radiant Energy
40 System (CERES), our PAR product was found to be a more accurate dataset with higher
41 resolution. This new dataset is now available
42 at <https://doi.org/10.11888/RemoteSen.tpd.271909> (Tang, 2021).

43 **Keywords:** PAR; Dataset; High-resolution; Long-term



44 **1. Introduction**

45 Plants rely on chlorophyll to absorb solar radiation in the visible wavelength range
46 (400–700 nm) for photosynthesis (Huang et al., 2020), and sunlight in this band is
47 commonly referred to as photosynthetically active radiation (PAR). Thus, PAR is the
48 source of energy for biomass formation and may directly affect the growth,
49 development, yield, and product quality of vegetation (Zhang et al., 2014; Ren et al.,
50 2021), modulating energy exchange between Earth’s surface and the atmosphere
51 (Zhang et al., 2021). Therefore, a high-quality PAR dataset is indispensable for studies
52 of ecosystems, agriculture, and global change (Frouin et al., 2018).

53 However, measurements of PAR are not routinely conducted at weather stations
54 or radiation stations. For example, PAR is not routinely observed at the Baseline
55 Surface Radiation Network (BSRN, Ohmura et al., 1998) or at the China
56 Meteorological Administration (CMA, Tang et al., 2013) weather/radiation stations.
57 Long-term PAR observations are only provided by a few ecological experimental
58 observation networks, such as the Chinese Ecosystem Research Network (CERN, Wang
59 et al., 2016), the AmeriFlux network (<https://ameriflux.lbl.gov/>), the SURFace
60 RADiation budget network (SURFRAD,
61 <https://www.esrl.noaa.gov/gmd/grad/surfrad/>), and the National Ecological
62 Observatory Network (NEON, <https://www.neonscience.org/>). To compensate for the
63 lack of PAR observations, a number of methods have been developed over recent
64 decades to estimate PAR. These methods can be roughly divided into two categories:
65 station-based methods and satellite-based methods (Tang et al., 2017).

66 Station-based methods mainly estimate PAR using other available variables
67 measured at stations using empirical or physical methods. Empirical methods usually
68 use the observed PAR and other variables to build an empirical relationship to conduct



69 PAR estimation. One such method is the well-known power law equation, which
70 usually uses the cosine of the solar zenith angle and the clearness index as inputs. The
71 clearness index, defined as the ratio of the solar radiation at the surface to that at the top
72 of the atmosphere (TOA), roughly reflects the solar light attenuation degree caused by
73 clouds, aerosols, water vapor, and other atmospheric compositions. A number of such
74 empirical methods based on the power law equation have been developed in the last
75 two decades (Alados et al., 1996; Xia et al., 2008; Hu et al. 2010; Hu and Wang 2014;
76 Yu et al. 2015; Wang et al., 2015, 2016). In addition, artificial neural network (ANN)
77 methods have also been used to estimate PAR from surface solar radiation (SSR) and
78 other meteorological variables (e.g., air temperature, relative humidity, dew point,
79 water vapor pressure, and air pressure) in a variety of ecosystems in China (Wang et al.,
80 2016). Generally, the aforementioned empirical methods can work well when calibrated
81 with local PAR observations, but the parameters in these methods are station-dependent
82 and their performance at locations where observations are not available will deteriorate.

83 Physical methods of PAR estimation generally consider various attenuations in the
84 atmosphere through parameterization approximation to complicated radiative transfer
85 processes. For example, Gueymard (1989a, 1989b, 2008) developed three physical
86 methods for the estimation of PAR, but these only work under clear-sky conditions. To
87 obtain all-sky PAR, Qin et al. (2012) further extended these methods to cloudy skies by
88 importing the measurements of sunshine duration that are usually conducted at most
89 meteorological stations. Tang et al. (2013) used the PAR method of Qin et al. (2012) to
90 estimate the daily PAR at more than 700 CMA routine weather stations, and found its
91 accuracy was comparable to those of local calibrated methods. Nevertheless, the PAR
92 method of Qin et al. (2012) can only be used to estimate daily PAR, and strictly can
93 only be applied at weather stations where the observation of sunshine duration is



94 available.

95 Alternatively, satellite-based methods can be used to map spatially continuous
96 PAR, but compared to SSR, little attention has been paid to PAR estimation using
97 remote sensing data (Van Laake and Sanchez-Azofeifa, 2004; Liang et al., 2006). There
98 are a few algorithms for estimating PAR using satellite data, and these algorithms may
99 be grouped into two categories: methods based on look-up tables (LUTs) based and
100 parameterization methods.

101 LUT-based methods can circumvent complicated radiative transfer calculations
102 (Huang et al., 2019) to estimate PAR directly from the satellite’s signal by searching
103 pre-calculated LUTs. Since first proposed by Pinker and Laszlo (1992), several similar
104 LUT-based methods (Liang et al., 2006; Zhang, et al., 2014; Huang, et al., 2016) have
105 emerged to estimate PAR from regional to global scales with different satellite sources.
106 However, LUT-based methods are more vulnerable to various uncertainties due to their
107 “black-box” nature, and they are also difficult to port across different satellite platforms.

108 In contrast, parameterization methods do not rely on satellite platforms.
109 Essentially, they comprise a simplification of the radiative transfer processes, and thus
110 require various land and atmospheric products from satellite retrievals as inputs to
111 estimate PAR. To some extent, the accuracy of these methods depends on the accuracy
112 of the input data. On the other hand, the uncertainty of parameterization methods comes
113 mainly from the treatment of clouds; this is because the clear-sky part of the method is
114 relatively mature with uncertainty less than 10% compared with the rigorous radiative
115 transfer calculation (Huang et al., 2020). There has been little attention paid to specific
116 cloud parameterization for PAR estimation except for the work of Van-Laake and
117 Sanchez-Azofeifa (2004), Sun et al. (2017), and Huang et al. (2020). Sun et al. (2017)
118 used one (UV–visible) of their two broadbands (UV–visible and near infrared) model



119 (a physical-based parameterization scheme for the estimation of SSR), to estimate all-
120 sky PAR. By further considering the multiple scattering and reflection of clouds, Huang
121 et al. (2020) developed a more complicated cloud parameterization scheme and
122 combined this with the clear-sky PAR model of Gueymard (1989a) to estimate all-sky
123 PAR. Although their accuracies are both acceptable, there is no corresponding PAR
124 product currently being produced for relevant scientific research.

125 In the past, a few global PAR products have been developed, such as the global
126 gridded PAR products of the International Satellite Cloud Climatology Project (ISCCP-
127 PL, Pinker and Laszlo, 1992), the Clouds and the Earth's Radiant Energy System
128 (CERES, Su et al., 2007), the Global Land Surface Satellite products (GLASS, Zhang
129 et al. 2014), the MODIS (MCD18A2 product, Wang et al., 2020), the Breathing Earth
130 System Simulator (BESS, Ryu et al., 2018), and a product from Hao et al. (2019) based
131 the observations from the Earth Polychromatic Imaging Camera (EPIC) onboard the
132 Deep Space Climate Observatory (DSCOVR, Burt and Smith, 2012). However, these
133 global PAR products are either too coarse in spatial resolution to meet refined analyses,
134 too low in temporal resolution to reflect daily variations, or too short in time series to
135 meet the demand of climate change studies. As a result, a high-resolution long-term
136 global gridded PAR product is urgently needed in the scientific community.

137 In this study, a high-resolution 35-year global gridded PAR product was developed
138 using an effective physical PAR estimation model, driven mainly by the latest high-
139 resolution ISCCP H-series cloud products, the aerosol product of the Modern-Era
140 Retrospective analysis for Research and Applications, Version 2 (MERRA-2) reanalysis
141 data, and water vapor, surface pressure, and ozone amount products of the ERA5
142 reanalysis data. We also evaluated the performance of our PAR product using in-situ
143 observations measured across three experimental observation networks in the United



144 States and China, and compared its performance with another common global satellite
145 product. The rest of the article is organized as follows. In Section 2, we introduce the
146 method used to map the global gridded PAR product. The input data for estimating the
147 global gridded PAR product, and the in-situ data for evaluating the performance of our
148 estimated global gridded PAR product are described in Section 3. Section 4 presents
149 the validation results of our global gridded PAR product and compares this with the
150 well-known satellite-based global PAR product of CERES. Section 5 describes data
151 availability, and our summary and conclusions are given in Section 6.

152

153 **2 Estimation of PAR**

154 The algorithm used to map global gridded PAR in this study was the
155 parameterization method developed by Tang et al. (2017), who combined the physical-
156 based clear-sky PAR model of Qin et al. (2012) and the parameterization scheme for
157 cloud transmittance of Sun et al. (2012). In calculating the surface PAR, the algorithm
158 takes into account various attenuation processes in the atmosphere, such as absorption
159 of water vapor and ozone, Rayleigh scattering, and absorption and scattering of cloud
160 and aerosol. In addition, the algorithm also considers the multiple reflections between
161 the surface and the atmosphere. The parametric expressions for the PAR algorithm are
162 all converted from the extensive radiative transfer calculations, and thus it is a physical
163 and efficient method that does not require calibration with ground-based observations.

164 The inputs of the PAR algorithm mainly include aerosol optical depth, cloud
165 optical depth, water vapor, ozone amount, surface albedo, and surface air pressure.
166 Tang et al. (2017) used the developed PAR algorithm to estimate instantaneous PAR
167 using the atmosphere and land products of the Moderate Resolution Imaging
168 Spectroradiometer (MODIS), and the estimated instantaneous PAR was evaluated



169 against in-situ observations collected by the SURFRAD network. It was found that this
170 algorithm performs better than previous algorithms and the estimated instantaneous
171 PAR can have a root mean square error (RMSE) of about 40 W m^{-2} . Therefore, we
172 expect good performance from our algorithm in mapping global gridded PAR.
173 Interested readers can refer to our earlier article (Tang et al., 2017) for further details.

174

175 **3 Data**

176 **3.1 Input data**

177 To produce a long-term (from 1984 to 2018) high-resolution global gridded PAR
178 product using the PAR algorithm presented above, we used input data from four
179 different sources.

180 The first source of input data was the latest level-2 H-series pixel-level global
181 (HXG) cloud products of the ISCCP, here referred to as ISCCP-HXG; these were
182 publicly available, spanned the period July 1983 to December 2018, had a spatial
183 resolution of 10 km, and a temporal resolution of 3 hours. The ISCCP-HXG cloud
184 products were produced by a series of cloud-related algorithms based on global gridded
185 two-channel radiance data (visible, $0.65 \mu\text{m}$ and infrared, $10.5 \mu\text{m}$) merged from
186 different geostationary and polar orbiting meteorological satellites. We must bear in
187 mind that the 3-hour ISCCP-HXG cloud products denote instantaneous data at a given
188 moment every three hours, not a mean of 3 hours. We used four variables from the
189 ISCCP-HXG cloud products; these were cloud mask, cloud top temperature, and the
190 optical depths of water cloud or ice cloud retrieved based on the visible radiance. The
191 sky condition (clear or cloudy) of a pixel was distinguished by the cloud mask data, and
192 the cloud phase (liquid or ice) of a cloudy pixel was roughly determined by the cloud
193 top temperature. If the cloud top temperature (TC) of a cloudy pixel was greater than



194 or equal to 253.1 K, it was regarded as water cloud; otherwise, it was classed as ice
195 cloud. For more detailed information on the ISCCP-HXG cloud products, the reader
196 may refer to the cloud products article of Young et al. (2018).

197 The second source of input data was the aerosol product of the MEERA-2
198 reanalysis data, which can be downloaded from the Goddard Earth Sciences Data and
199 Information Services Center of the National Aeronautics and Space Administration
200 (NASA). MERRA-2 assimilates ground-observed aerosol optical depth (AOD)
201 measured at the AERONET (Holben et al., 1998), and satellite-retrieved AOD from the
202 MODIS Aqua and Terra sensors, MISR sensor, and AVHRR sensor (Randles et al.
203 2017). The MERRA-2 hourly aerosol product used in this study was called
204 “avg1_2d_aer_Nx”, having a spatial resolution of $0.5^\circ \times 0.625^\circ$, a temporal resolution
205 of 1 hour, and a time period of 1980 to present. Two variables of the MERRA-2 aerosol
206 product were used in this study; these were the total AOD at 550 nm and the total
207 aerosol Ångström parameter (470–870 nm). To map the global gridded PAR product
208 with a spatial resolution of 10 km, we re-sampled the MERRA-2 aerosol product to a
209 spatial resolution of 10 km.

210 The third source of input data was the routine weather variables of the ERA5
211 reanalysis data, which mainly included total column ozone, total column water vapor,
212 and surface pressure, with a spatial resolution of 25 km and a temporal resolution of 1
213 hour. Total column ozone and total column water vapor were used to calculate the
214 transmittance due to ozone absorption and water vapor absorption, respectively.
215 Surface pressure was used to calculate the Rayleigh scattering in the atmosphere. To
216 maintain consistency with the spatial resolution of the ISCCP-HXG cloud product,
217 these three routine weather variables of the ERA5 reanalysis data were re-sampled to
218 10 km.



219 The fourth source of input data was albedo data from the MODIS MCD43A3
220 product (Schaaf et al., 2002) and from the Satellite Application Facility on Climate
221 Monitoring (CM-SAF) (CLARA-A2-SAL, Karlsson et al., 2017), to take into account
222 the multiple scattering effect between the land surface and atmosphere on the
223 calculation of PAR. The spatial resolutions of MODIS and CM-SAF were both 5 km,
224 and thus we downscaled them to 10 km. The MODIS albedo product was used after
225 2000, the date when it first became available, and the CM-SAF albedo product was
226 used before 2000 (when MODIS was unavailable). The use of different albedo products
227 will lead to inconsistent accuracy for the final global gridded PAR product, and thus
228 thus caution should be exercised when performing trend analyses.

229

230 **3.2 In-situ measurements**

231 In-situ PAR measurements collected across three networks from the United States
232 and China were used to validate our global gridded PAR product. PAR measurements
233 at those networks are all quantified as photosynthetic photo flux density ($\mu \text{ mol m}^{-2} \text{ s}^{-1}$),
234 and McCree's conversion factor with a value of approximately 4.6 (McCree, 1972)
235 was used to convert the quantum units of PAR into energy units (W m^{-2}) of PAR. The
236 first network used was SURFRAD (Augustine et al., 2000) of the National Oceanic and
237 Atmospheric Administration (NOAA), which contains seven experimental stations
238 (Goodwin Greek, Fort Peek, Bondville, Desert Rock, Sioux Falls, Table Mountain, and
239 Penn State) in different climatic regions (red pentagrams in Fig. 1). LI-COR Quantum
240 sensors were used to measure PAR at the SURFRAD network. The standards of
241 instrument calibration for the Baseline Surface Radiation Network (BSRN) were
242 adopted and the quality of radiation data at SURFRAD were considered to be
243 comparable to those of the BSRN. Many previous studies have used SURFRAD



244 radiation data to evaluate their algorithms for estimation of different radiation
245 components. The PAR observations at 1-minute temporal resolution from 2009 to 2016
246 at the seven SURFRAD stations were used.

247 The second network used was NEON (Metzger et al., 2019), and 42 terrestrial
248 tower stations (denoted by red triangles in Fig. 1) in the network were used in this study.
249 Generally, measurements of the PAR vertical profile at multiple vertical levels were
250 conducted at each tower station and the tower-top PAR measurements were used to
251 validate our global gridded PAR product. Kipp & Zonen PQS 1 quantum sensors with
252 an uncertainty within 4% (Blonquist and Johns, 2018) were used to measure PAR across
253 the NEON. The sensors sampled with frequency of 1 Hz, recorded PAR values every
254 minute, and were calibrated every year. The starting times of PAR observations at the
255 42 NEON stations are different to each other, and thus here we used PAR observations
256 from the starting time of each site to the end of 2018.

257 The third network used was CERN, and 38 stations (marked with red circles in Fig.
258 1) across diverse terrestrial ecosystems were used in this study. These 38 CERN stations
259 were distributed across different climatic zones and belonged to eight different
260 ecosystems: agriculture, forest, desert, marine, grassland, lake, marsh wetland, and
261 urban. LI-190SA quantum sensors with an uncertainty of approximately 5% (Hu et al.,
262 2007) were used to measure PAR across CERN, and the spectrometer and standard
263 radiative lamp were adopted to centralized calibrate and compare among the quantum
264 sensors. The PAR observations were recorded hourly and thus we only validated our
265 daily PAR product against CERN due to the mismatch between the hourly observed
266 data and the satellite-based instantaneous retrievals. The daily mean PAR datasets from
267 the 38 CERN stations from 2005 to 2015 were publicly shared by Liu et al. (2017) and
268 used herein.



269 **4 Results and Discussion**

270 Based on the above inputs and the physical-based PAR algorithm, we produced a
271 long-term (from 1984 to 2018) high resolution (10 km spatial resolution and 3 hours
272 temporal resolution) global gridded PAR product, here referred to as the ISCCP-ITP
273 PAR product. In-situ observations from three networks were used to evaluate the
274 performance of our ISCCP-ITP PAR product at instantaneous and daily scales. In
275 addition, a widely used global gridded PAR product of the CERES (SYN1deg-1hour,
276 edition 4A), with a spatial resolution of $1^\circ \times 1^\circ$ and a temporal resolution of 1 hour, was
277 used to provide a comparison with our ISCCP-ITP PAR product. To discuss the
278 influence of spatial resolution on the accuracy of our global gridded PAR product, we
279 also evaluated the estimated PAR at different spatial resolutions from 10 km to 110 km.
280 The estimated PAR at spatial resolutions from 30 km to 110 km were calculated by
281 averaging the corresponding original PAR at the 10 km scale. Here, the three statistical
282 metrics of mean bias error (MBE), RMSE, and correlation coefficient (R), were used to
283 evaluate the performance of our ISCCP-ITP PAR product and the CERES PAR product.
284

285 **4.1 Validation of instantaneous PAR**

286 In this study, the instantaneous PAR was validated against the observed hourly
287 PAR, which was calculated by averaging the 1-minute PAR over the time period of 30
288 minutes before and after satellite overpass. Our estimated instantaneous PAR was firstly
289 validated against in-situ data measured at the seven SURFRAD stations. Figure 2
290 presents the validation results for the instantaneous PAR at spatial resolutions of 10 km
291 and 30 km, and the validation result for the CERES hourly PAR with a spatial resolution
292 of approximately 100 km. It can be seen that the accuracy of the instantaneous PAR at
293 10 km spatial resolution (MBE = 5.6 W m^{-2} , RMSE = 44.3 W m^{-2} , $R = 0.94$) is



294 comparable to that of the CERES hourly PAR at 100 km spatial resolution (MBE = 4.9
295 W m^{-2} , RMSE = 44.1 W m^{-2} , $R = 0.93$). However, when the instantaneous PAR at 10
296 km spatial resolution was averaged to 30 km, its accuracy was markedly improved;
297 RMSE decreased from 44.3 to 36.3 W m^{-2} and R increased from 0.94 to 0.96, and thus
298 its accuracy at 30 km spatial resolution is clearly higher than that of the CERES product.

299 Table 1 shows the accuracies of our estimated instantaneous PAR at different
300 spatial resolutions from 10 km to 110 km. It can be seen that the accuracy at the original
301 10 km spatial resolution was clearly lower than at all other resolutions (30–110 km),
302 and the accuracy was highest at a resolution of 50–70 km. This may be due to the
303 following two reasons. Firstly, the representativeness of ground-based observational
304 stations may be greater than 10 km. Secondly, there is time mismatch between satellite-
305 based and surface-based observations because the last generation of geostationary
306 meteorological satellites (e.g., the Geostationary Operational Environmental Satellite
307 (GOES)) require approximately half an hour to complete a disk scan. Spatially
308 averaging the instantaneous PAR to a larger area could partially eliminate this time
309 mismatch.

310 The instantaneous PAR was also evaluated against the 42 NEON stations (Figure
311 3 and Table 2). The performance against NEON was slightly worse than that against
312 SURFRAD. At the 10 km scale, the former produced a 1.2 W m^{-2} larger RMSE than the
313 latter, and both produced a positive MBE of approximately 6 W m^{-2} and R of 0.94.
314 Similar to the situation at SURFRAD, the accuracy at NEON was markedly improved
315 at 30 km spatial resolution, reached a peak at 50 km resolution, and then started to
316 decrease slightly at 70 km resolution. Compared to the performance of the CERES
317 hourly PAR at NEON, the accuracy of our estimated instantaneous PAR was higher at
318 all scales from 10 km to 110 km. More importantly, the spatial resolution of our PAR



319 product (10 km) is much finer than that of the CERES PAR product (100 km).

320 Due to the significant improvement when our estimated PAR was upscaled to 30
321 km spatial resolution, we used a 3×3 spatial window to smooth the raw PAR to derive
322 our final global grided PAR product. Thus, we here present the spatial distributions of
323 MBE and RMSE (Figure 4) for our estimated PAR with a spatial resolution of 30 km
324 across seven SURFRAD and 42 NEON stations in the USA. The MBE values range
325 from -11.2 to 19.8 W m^{-2} , with a negative MBE at 5 of the 49 stations. From an MBE
326 point of view, 42 stations fall into the range -10 to 10 W m^{-2} , and among these 22
327 stations fall within -5 to 5 W m^{-2} . The RMSE values range from 24.2 to 52.3 W m^{-2} ,
328 with $\text{RMSE} \leq 35 \text{ W m}^{-2}$ at 18 stations, RMSE between 35 and 40 W m^{-2} at 19 stations,
329 RMSE between 40 and 50 W m^{-2} at 12 stations, and $\text{RMSE} > 50 \text{ W m}^{-2}$ at only one
330 station. The largest MBE and RMSE both occur at the Great Smoky Mountains National
331 Park (GRSM) station, which is situated in the mountains of southeastern Tennessee.
332 Similar large errors at this station were also found for the CERES PAR product. The
333 relatively large errors at this station could be caused by the poor representativeness of
334 the mountain observational station.

335

336 **4.2 Validation of daily PAR**

337 Our estimated daily PAR (ISCCP-ITP) was derived by averaging the instantaneous
338 PAR of eight moments in the day, and validated against the three networks of
339 SURFRAD, NEON, and CERN. Similar to the validation results for the instantaneous
340 PAR, the performance of our estimated daily PAR at 10 km spatial resolution was
341 comparable to that of the CERES product at SURFRAD and NEON, and when upscaled
342 to ≥ 30 km, our daily PAR product performed slightly better than that of CERES.
343 Therefore, here we do not give validation results for the CERES daily PAR at



344 SURFRAD and NEON, but only give validation results for the CERES daily PAR at
345 CERN.

346 Validation results for our estimated daily PAR against in-situ data collected at
347 SURFRAD are shown in Figure 5 and Table 3. The MBE, RMSE, and R values were
348 0.4 W m^{-2} , 13.2 W m^{-2} , and 0.96, respectively, for daily PAR at 10 km spatial resolution.
349 When upscaled to 30 km spatial resolution, these statistical metrics changed to 0.6 W
350 m^{-2} , 11.2 W m^{-2} , and 0.97, respectively. When upscaled to $\geq 50 \text{ km}$, the RMSE gradually
351 decreased to approximately 10 W m^{-2} . The MBE and R changed to 0.5 W m^{-2} and 0.98,
352 respectively.

353 Validation results for our estimated daily PAR against NEON are shown in Figure
354 6 and Table 4. The RMSE for daily PAR at 10 km spatial resolution was 13.1 W m^{-2} ,
355 and this value decreased to 11.6 W m^{-2} for 30 km spatial resolution. The R for daily
356 PAR was 0.96 and 0.97 for 10 km and 30 km spatial resolution, respectively. When
357 upscaled to $\geq 50 \text{ km}$, these statistical metrics remained almost unchanged. The
358 performance against NEON is comparable to that against SURFRAD for our daily PAR
359 product.

360 Figure 7 shows the spatial distributions of MBE and RMSE for our estimated daily
361 PAR with a spatial resolution of 30 km against seven SURFRAD and 42 NEON stations
362 in the USA. The largest negative and positive MBE values were -5.3 W m^{-2} and 9.3 W
363 m^{-2} , respectively. There were seven stations with $\text{MBE} < 0 \text{ W m}^{-2}$, 41 stations with
364 MBE values between -5 W m^{-2} and 5 W m^{-2} , 31 stations with MBE values between -3
365 W m^{-2} and 3 W m^{-2} , and only eight stations with absolute $\text{MBE} > 5 \text{ W m}^{-2}$. The largest
366 and smallest RMSE values were 17.6 W m^{-2} , and 6.9 W m^{-2} , respectively. There were
367 12 stations with $\text{RMSE} < 10 \text{ W m}^{-2}$, 19 stations with RMSE between 10 W m^{-2} and 12
368 W m^{-2} , 12 stations with RMSE between 12 W m^{-2} and 13 W m^{-2} , and only six stations



369 with $RMSE > 13 \text{ W m}^{-2}$. Likewise, the largest MBE and RMSE values were found at
370 the GRSM station with the main reason again likely being due to the poor
371 representativeness of this station.

372 Finally, we validated our daily PAR and the CERES daily PAR products against
373 in-situ data collected across CERN (Figure 8). The performance of our daily PAR
374 product at the 10 km scale ($MBE = 1.4 \text{ W m}^{-2}$, $RMSE = 19.6 \text{ W m}^{-2}$, $R = 0.89$) was
375 slightly worse than that of the CERES daily PAR product ($MBE = -1.3 \text{ W m}^{-2}$, $RMSE$
376 $= 18.7 \text{ W m}^{-2}$, $R = 0.90$). However, when upscaled to $\geq 30 \text{ km}$, the accuracies of our
377 estimated daily PAR were comparable to, or slightly better than, those of the CERES
378 daily PAR. Another phenomenon we noticed was that the RMSEs against CERN data
379 were approximately $7\text{--}8 \text{ W m}^{-2}$ greater than those against SURFRAD and NEON data
380 for both our daily PAR and the CERES PAR products. This could be attributed to the
381 fact that the quality of PAR observations at CERN is slightly worse than that at
382 SURFRAD and NEON, but further evidence is required to support this speculation.
383 Another possible reason could be the effect of aerosols because aerosols are a major
384 attenuation factor affecting the clear-sky PAR (Qin et al., 2012; Tang et al. 2013).
385 Because the aerosol optical depth (AOD) over China is much greater than that over the
386 USA (Li et al., 2011), greater uncertainty in the aerosol data over China would lead to
387 larger errors in PAR estimation over China.

388 Figure 9 presents the spatial distributions of MBE and RMSE for our estimated
389 daily PAR with a spatial resolution of 30 km against the 38 CERN stations. The MBE
390 values at most of the stations were between -10 W m^{-2} and 10 W m^{-2} . The stations with
391 negative MBE were mainly located in northwestern China, and the stations with
392 positive MBE were mainly located in southeastern China. The RMSE values at most of
393 the stations were $< 23 \text{ W m}^{-2}$, and there were only five stations where the RMSE was $>$



394 25 W m^{-2} . Stations with an absolute MBE $> 10 \text{ W m}^{-2}$ were mainly located in four
395 forested areas (Beijing, Xishuangbanna, Heshan, and Ailao Mountain), one agricultural
396 area (Huanjiang), one lake area (Taihu), and one Desert area (Fukang). Likewise, the
397 RMSE values at these seven stations were relatively large. Similar large errors at these
398 stations were also found for the CERES PAR product. The large errors at these stations
399 could be caused by the poor representativeness at some mountain stations, large
400 uncertainty in the inputs at some stations, or uncertainty in observational data.

401

402 **4.3 Spatial distribution of multi-year average PAR**

403 Figure 10 shows the global spatial distribution of multi-year annual average PAR
404 (ISCCP-ITP) during the period 2001–2018, and comparison with that of the CERES
405 PAR is also shown. The spatial pattern of our ISCCP-ITP PAR product is quite
406 consistent with that of the CERES PAR product, whose spatial resolution was far
407 coarser than that of our PAR product. There were some finer patterns that the CERES
408 PAR product could not distinguish, but our PAR product could clearly capture. This
409 defect in the CERES PAR product was especially evident in mountainous areas, such
410 as the Tibetan Plateau. The annual average PAR was generally high in latitudinal zones
411 lying between 30° N and 30° S , and low in other regions. In addition, there were some
412 high-altitude regions with high PAR values, such as the Tibetan Plateau and Bolivian
413 Plateau.

414 Figure 11 displays the global spatial distributions of multi-year seasonal average
415 PAR (ISCCP-ITP) during the period 2001–2018. The four panels in the figure reflect
416 the process of seasonal change and exhibit different spatial distribution characteristics.
417 Compared to mid- and high-latitude areas, more PAR was received around the equator
418 and low latitudes (30° N – 30° S) in all four seasons. Over the latitudinal zone between



419 30° S and 90 ° S in southern hemisphere, PAR received by the surface gradually
420 increased from spring to winter, with the lowest values in spring and summer, a
421 relatively larger value in autumn, and the largest value in winter. Over the latitudinal
422 zone between 30° N and 90° N in northern hemisphere, the situation was very different.
423 PAR received by the surface was largest in summer, lowest in autumn and winter, and
424 intermediate in spring.

425

426 **5 Data availability**

427 Our long-term global gridded PAR product is available at the National Tibetan
428 Plateau Data Center (<https://doi.org/10.11888/RemoteSen.tpdc.271909>, Tang, 2021),
429 Institute of Tibetan Plateau Research, Chinese Academy of Sciences.

430

431 **6 Summary and Conclusions**

432 A long-term (1984–2018) global high-resolution (10 km spatial resolution, 3 h
433 temporal resolution) gridded PAR product was produced using our previously published
434 physical-based PAR parametrization scheme. The main inputs for this PAR model were
435 the latest ISCCP H-series cloud product, ERA5 routine meteorological data (water
436 vapor, surface pressure, and ozone), MERRA-2 aerosol product, and albedo products
437 from MODIS (after 2000) and CLARRA-2 (before 2000). The generated PAR product
438 was validated globally against in-situ data measured across three observational
439 networks in the USA and China. For the instantaneous PAR at original the scale (10
440 km), the overall MBE, RMSE, and R were 5.8 W m⁻², 44.9 W m⁻² and 0.94, respectively.
441 When smoothed to ≥ 30 km, the accuracy was markedly improved, with RMSE
442 decreasing to 37.1 W m⁻² and R increasing to 0.96. For the daily PAR at spatial
443 resolutions of 10 km and 30 km, the RMSE values were approximately 13.1 W m⁻² and



444 11.4 W m^{-2} , respectively, in the USA. Validation results in China showed a greater
445 RMSE than in the USA. Due to the marked improvement when our PAR products were
446 upscaled to $\geq 30 \text{ km}$, we applied a 3×3 spatial smoothing window to the original PAR
447 data to produce the final PAR product.

448 Our estimated PAR product was also compared with the CERES PAR product; we
449 found that the accuracy of our estimated PAR product at the original scale (10 km) was
450 generally comparable to, or higher than, that of the CERES PAR product. When it was
451 upscaled to $\geq 30 \text{ km}$, the accuracy advantage of our product over the CERES PAR
452 product became more evident. Another clear advantage of our PAR product was the
453 increased spatial resolution it offered compared to the CERES PAR product. We expect
454 that our PAR product will contribute to the future understanding and modeling of the
455 global carbon cycle and ecological processes. In future work, we will attempt to
456 separate the components of direct and diffuse PAR from the total PAR because light use
457 efficiency is mainly controlled by diffuse PAR.

458

459 **Author contributions.** All authors discussed the results and contributed to the
460 manuscript. WT calculated the dataset, analyzed the results, and drafted the manuscript.

461

462 **Competing interests.** The authors declare that they have no conflicts of interest.

463

464 **Acknowledgments.** The in-situ observations of PAR at CERN were shared by Liu et
465 al. (2017) and are available online via <http://www.sciencedb.cn/dataSet/handle/326>.
466 The observed PAR data at SURFRAD and NEON are available online from their
467 official websites (<https://www.esrl.noaa.gov/gmd/grad/surfrad/> and
468 <http://data.neonscience.org>). The ISCCP H-series cloud products were provided by the



469 NOAA's National Centers for Environmental Information (NCEI). The ERA5 routine
470 weather data, MODIS albedo data, and MERRA-2 aerosol data are available from their
471 official websites (<https://www.ecmwf.int>, <https://ladsweb.modaps.eosdis.nasa.gov>, and
472 <https://gmao.gsfc.nasa.gov/reanalysis/MERRA-2/>). The authors would like to thank the
473 staff members at these observational networks and data production centers for their
474 valuable work.

475

476 **Financial support.** This work was supported by the National Key Research and
477 Development Program of China (Grant No. 2017YFA0603604), and the National
478 Natural Science Foundation of China (Grant No. 42171360).

479

480 **References**

481 Alados, I., Foyo-Moreno, I., Alados-Arboledas, L., 1996. Photosynthetically active
482 radiation: measurements and modelling. *Agric. For. Meteorol.* 78, 121–131.
483 [http://dx.doi.org/10.1016/0168-1923\(95\)02245-7](http://dx.doi.org/10.1016/0168-1923(95)02245-7).

484 Augustine, J.A., DeLuisi, J.J., Long, C.N., 2000. SURFRAD—A national surface
485 radiation budget network for atmospheric research. *Bull. Am. Meteorol. Soc.* 81,
486 2341–2357. [https://doi.org/10.1175/1520-
487 0477\(2000\)081<2341:SANSRB>2.3.CO;2](https://doi.org/10.1175/1520-0477(2000)081<2341:SANSRB>2.3.CO;2).

488 Blonquist, M., Johns, J., 2018. Accurate PAR Measurement: Comparison of Eight
489 Quantum Sensor Models. [https://www.apogeeinstruments.
490 com/content/Comparison-of-Eight-Quantum-Sensor-Models.pdf](https://www.apogeeinstruments.com/content/Comparison-of-Eight-Quantum-Sensor-Models.pdf).

491 Burt, J., Smith, B., 2012. Deep space climate observatory: the DSCOVR mission. *IEEE
492 Aerosp. Conf. Proc.* <https://doi.org/10.1109/AERO.2012.6187025>.

493 Frouin, R., Ramon, D., Boss, E., Jolivet, D., Compi`egne, M., Tan, J., Bouman, H.,



- 494 Jackson, T., Franz, B., Platt, T., Sathyendranath, S., 2018. Satellite radiation
495 products for ocean biology and biogeochemistry: needs, state-of-the-art, gaps,
496 development priorities, and opportunities. *Front. Mar. Sci.* 5, 1–20. [https://doi.org/](https://doi.org/10.3389/fmars.2018.00003)
497 10.3389/fmars.2018.00003.
- 498 Gueymard, C., 1989a. An atmospheric transmittance model for the calculation of the
499 clear sky beam, diffuse and global photosynthetically active radiation. *Agric. For.*
500 *Meteorol.* 45, 215–229. [http://dx.doi.org/10.1016/0168-1923\(89\)90045-2](http://dx.doi.org/10.1016/0168-1923(89)90045-2).
- 501 Gueymard, C., 1989b. A two-band model for the calculation of clear sky solar irradiance,
502 illuminance, and photosynthetically active radiation at the earth’s surface. *Sol.*
503 *Energy* 43, 253–265. [http://dx.doi.org/10.1016/0038-092X\(89\)90113-8](http://dx.doi.org/10.1016/0038-092X(89)90113-8).
- 504 Gueymard, C.A., 2008. REST2: High-performance solar radiation model for cloudless-
505 sky irradiance, illuminance, and photosynthetically active radiation—Validation
506 with a benchmark dataset. *Sol. Energy* 82, 272–285.
507 <http://dx.doi.org/10.1016/j.solener.2007.04.008>.
- 508 Hao, D., Asrar, G.R., Zeng, Y., Zhu, Q., Wen, J., Xiao, Q., Chen, M., 2019. Estimating
509 hourly land surface downward shortwave and photosynthetically active radiation
510 from DSCOVR/EPIC observations. *Remote Sens. Environ.* 232, 111320.
511 <https://doi.org/10.1016/j.rse.2019.111320>.
- 512 Holben, B.N., Eck, T.F., Slutsker, I., Tanre, D., Buis, J.P., Setzer, A., Vermote, E.,
513 Reagan, J.A., Kaufman, Y.J., Nakajima, T., Lavenu, F., Jankowiak, I., Smirnov, A.,
514 1998. AERONET—a federated instrument network and data archive for aerosol
515 characterization. *Remote Sens. Environ.* 66, 1–16. [https://doi.org/10.1016/S0034-](https://doi.org/10.1016/S0034-4257(98)00031-5)
516 4257(98)00031-5.
- 517 Hu, B., Wang, Y., Liu, G., 2007. Spatiotemporal characteristics of photosynthetically
518 active radiation in China. *J. Geophys. Res.* 112 (D14).



- 519 <http://dx.doi.org/10.1029/2006JD007965>.
- 520 Hu, B., Wang, Y., Liu, G., 2010. Long-term trends in photosynthetically active radiation
521 in Beijing. *Adv. Atmos. Sci.* 27, 1380–1388. [http://dx.doi.org/10.1007/s00376-](http://dx.doi.org/10.1007/s00376-010-9204-2)
522 010-9204-2.
- 523 Hu, B., Wang, Y., 2014. Comparison of multi-empirical estimation models of
524 photosynthetically active radiation under all sky conditions in Northeast China.
525 *Theor. Appl. Climatol.* 116, 119–129. [http://dx.doi.org/10.1007/s00704-013-0941-](http://dx.doi.org/10.1007/s00704-013-0941-x)
526 x.
- 527 Huang, G. H., Li, X., Ma, M. G., Li, H. Y., and Huang, C. L., 2016. High resolution
528 surface radiation products for studies of regional energy, hydrologic and ecological
529 processes over Heihe river basin, northwest China, *Agricultural and Forest*
530 *Meteorology*, vol. 230, pp. 67-78.
- 531 Huang, G., Li, Z., Li, X., Liang, S., Yang, K., Wang, D., and Zhang, Y., 2019: Estimating
532 surface solar irradiance from satellites: Past, present, and future perspectives.
533 *Remote Sensing of Environment*, 233, 111371.
- 534 Huang, G. H., Li, X., Lu, N., Wang, X., and He, T., 2020. A General Parameterization
535 Scheme for the Estimation of Incident Photosynthetically Active Radiation under
536 Cloudy Skies, *IEEE Trans. Geosci. Remote Sens.*, vol. 58 (9), pp. 6255 – 6265.
- 537 Karlsson, Karl-Göran; Anttila, Kati; Trentmann, Jörg; Stengel, Martin; Meirink, Jan
538 Fokke; Devasthale, Abhay; Hanschmann, Timo; Kothe, Steffen; Jääskeläinen,
539 Emmihenna; Sedlar, Joseph; Benas, Nikos; van Zadelhoff, Gerd-Jan; Schlundt,
540 Cornelia; Stein, Diana; Finkensieper, Stephan; Håkansson, Nina; Hollmann,
541 Rainer; Fuchs, Petra; Werscheck, Martin (2017): CLARA-A2: CM SAF cLOUD,
542 Albedo and surface RAdiation dataset from AVHRR data - Edition 2, Satellite
543 Application Facility on Climate Monitoring,



- 544 DOI:10.5676/EUM_SAF_CM/CLARA_AVHRR/V002, <https://doi.org/10.5676/>
545 EUM_SAF_CM/CLARA_AVHRR/V002.
- 546 Li, Z., et al. (2011), East Asian Studies of Tropospheric Aerosols and their Impact on
547 Regional Climate (EAST-AIRC): An overview, *J. Geophys. Res.*, 116, D00K34,
548 doi:10.1029/2010JD015257.
- 549 Liang, S., Zheng, T., Liu, R. G., Fang, H. L., Tsay, S. C., and Running, S.: Estimation
550 of incident photosynthetically active radiation from Moderate Resolution Imaging
551 Spectrometer data, *J. Geophys. Res.*, 111, D15208, doi:10.1029/2005JD006730,
552 2006.
- 553 Liu, H., et al., (2017), CERN photosynthetically active radiation dataset from 2005 to
554 2015, *China Scientific Data*, 2017, 2(1), 1 – 10. DOI:
555 10.11922/csdata.170.2016.0100.
- 556 McCree, K.J., 1972. Test of current definitions of photosynthetically active radiation
557 against leaf photosynthesis data. *Agric. Meteorol.* 10, 443-453.
558 [http://dx.doi.org/10.1016/0002-1571\(72\)90045-3](http://dx.doi.org/10.1016/0002-1571(72)90045-3).
- 559 Metzger S, Ayres E, Durden D, Florian C, Lee R, Lunch C, Luo H, Pingintha-Durden
560 N, Roberti JA, SanClements M, Sturtevant C, Xu K, Zulueta RC (2019) From
561 NEON field sites to data portal: a community resource for surface–atmosphere
562 research comes online. *Bull Am Meteorol Soc* 100 (11):2305–2325.
- 563 Ohmura, A., et al.: Baseline Surface Radiation Network (BSRN/WCRP): New
564 precision radiometry for climate change research, *Bull. Am. Meteorol. Soc.*, 79,
565 2115 – 2136, doi:10.1175/1520-0477(1998)079<2115:BSRNBW>2.0.CO;2, 1998.
- 566 Pinker, R. T., and Laszlo, I., 1992. Global Distribution of Photosynthetically Active
567 Radiation as Observed from Satellites, *Journal of Climate*, vol. 5, pp. 56-65.
- 568 Qin, J., Yang, K., Liang, S., Tang, W., 2012. Estimation of daily photosynthetically



- 569 active radiation under all-sky conditions from sunshine duration data. *J. Appl.*
570 *Meteorol. Climatol.* 51:150–160. <http://dx.doi.org/10.1175/JAMC-D-10-05018.1>.
- 571 Randles, C.A., Silva, A.M.d., Buchard, V., Colarco, P.R., Darmenov, A., Govindaraju,
572 R., Smirnov, A., Holben, B., Ferrare, R., Hair, J., Shinozuka, Y., Flynn, C.J., 2017.
573 The MERRA-2 Aerosol Reanalysis, 1980 Onward. Part I: system description and
574 data assimilation evaluation. *J. Clim.* 30, 6823–6850. <https://doi.org/10.1175/jcli->
575 [d-16-0609.1](https://doi.org/10.1175/jcli-d-16-0609.1).
- 576 Ren, Y., Yang, K., Wang, H., Zhao, L., Chen, Y., Zhou, X., & La, Z. (2021). The South
577 Asia monsoon break promotes grass growth on the Tibetan Plateau. *Journal of*
578 *Geophysical Research: Biogeosciences*, 126, e2020JG005951.
579 <https://doi.org/10.1029/2020JG005951>.
- 580 Ryu, Y., Jiang, C., Kobayashi, H., Detto, M., 2018. MODIS-derived global land
581 products of shortwave radiation and diffuse and total photosynthetically active
582 radiation at 5 km resolution from 2000. *Remote Sens. Environ.* 204, 812–825.
583 <https://doi.org/10.1016/j.rse.2017.09.021>.
- 584 Schaaf, C. B., et al.: First operational BRDF, albedo nadir reflectance products from
585 MODIS, *Remote Sens. Environ.*, 83, 135–148, doi:10.1016/S0034-
586 4257(02)00091-3, 2002.
- 587 Su, W., Charlock, T.P., Rose, F.G., Rutan, D., 2007. Photosynthetically active radiation
588 from Clouds and the Earth’s Radiant Energy System (CERES) products. *J.*
589 *Geophys. Res. Biogeosci.* 112, 1–11. <https://doi.org/10.1029/2006JG000290>.
- 650 Sun, Z., Liu, J., Zeng, X., and Liang, H.: Parameterization of instantaneous global
651 horizontal irradiance: Cloudy sky component, *J. Geophys. Res.*, 117, D14202,
652 doi:10.1029/2012JD017557, 2012.
- 653 Sun, Z., Liang, H., Liu, J., and Shi, G., 2017. Estimation of photosynthetically active



- 654 radiation using solar radiation in the UV–visible spectral band. *Sol. Energy* 153,
655 611–622. <http://dx.doi.org/10.1016/j.solener.2017.06.007>.
- 656 Tang, W. (2021). A long-term and high-resolution global gridded photosynthetically
657 active radiation product (1984–2018). National Tibetan Plateau Data Center, DOI:
658 10.11888/RemoteSen.tpd.c.271909. CSTR: 18406.11.RemoteSen.tpd.c.271909.
- 659 Tang, W., Qin, J., Yang, K., Niu, X., Zhang, X., Yu Y., and Zhu X.: Reconstruction of
660 Daily Photosynthetically Active Radiation and its Trends over China, *J. Geophys.*
661 *Res. Atmos.*, 118(23), 13,292–13,302, doi:10.1002/2013JD020527, 2013.
- 662 Tang, W. J., Qin, J., Yang, K., Niu, X. L., Min, M., and Liang, S. L.: An efficient
663 algorithm for calculating photosynthetically active radiation with MODIS
664 products, *Remote Sensing of Environment*, vol. 194, pp. 146–154, 2017.
- 665 Van Laake, P.E., Sanchez -Azofeifa, G.A., 2004. Simplified atmospheric radiative
666 transfer modelling for estimating incident PAR using MODIS atmosphere
667 products. *Remote Sens. Environ.* 91, 98–113.
- 668 Wang, D., Liang, S., Zhang, Y., Gao, X., Brown, M.G.L., Jia, A., 2020. A new set of
669 MODIS land products (MCD18): downward shortwave radiation and
670 photosynthetically active radiation. *Remote Sens.* 12, 168.
671 <https://doi.org/10.3390/rs12010168>.
- 672 Wang, L., Gong, W., Feng, L., Lin, A., Hu, B., Zhou, M., 2015. Estimation of hourly
673 and daily photosynthetically active radiation in Inner Mongolia, China, from 1990
674 to 2012. *Int. J. Climatol.* 35, 3120–3131. <https://doi.org/10.1002/joc.4197>.
- 675 Wang, L., Kisi, O., Zounemat-Kermani, M., Hu, B., and Gong, W., Modeling and
676 comparison of hourly photosynthetically active radiation in different ecosystems.
677 *Renew Sust Energy Rev*, 2016, 56:436–453.
- 678 Xia, X., Li, Z., Wang, P., Cribb, M., Chen, H., Zhao, Y., 2008. Analysis of



679 photosynthetic photon flux density and its parameterization in Northern China.
680 Agric. For. Meteorol. 148 (6), 1101–1108.
681 <http://dx.doi.org/10.1016/j.agrformet.2008.02.008>.

682 Young, A.H., Knapp, K.R., Inamdar, A., Hankinns,W., and Rossow,W.B.: The
683 International Cloud Climatology Project H-Series climate data record product.
684 Earth Syst. Sci. Data, 10, 583–593, 2018.

685 Yu, X., Wu, Z., Jiang, W., Guo, X., 2015. Predicting daily photosynthetically active
686 radiation from global solar radiation in the Contiguous United States. Energy
687 Convers. Manage. 89, 71–82. <http://dx.doi.org/10.1016/j.enconman.2014.09.038>.

688 Zhang, H., Dong, X., Xi, B., Xin, X., Liu, Q., He, H., Xie, X., Li, L., and Yu, S.:
689 Retrieving high-resolution surface photosynthetically active radiation from the
690 MODIS and GOES-16 ABI data, Remote Sens. Environ., 260, 112436, 2021.

691 Zhang, X., Liang, S., Zhou, G., Wu, H., and Zhao, X.: Generating Global LAnd Surface
692 Satellite incident shortwave radiation and photosynthetically active radiation
693 products from multiple satellite data, Remote Sens. Environ., 152, 318 – 332, 2014.



694 **Figure captions**

695 **Figure 1** Distribution of observation stations within the three observation networks,
696 where measurements of PAR were carried out. The red circles denote the
697 locations of the 38 CERN stations, the red triangles denote the 42 NEON
698 stations, and the red pentagrams denote the seven SURFRAD stations.

699 **Figure 2** Comparisons of our estimated instantaneous PAR product (ISCCP-ITP) at
700 spatial resolutions of (a) 10 km, (b) 30 km, and (c) hourly PAR of the CERES
701 SYN1deg (edition 4.1) with observed PAR collected at seven SURFRAD
702 stations.

703 **Figure 3** Comparisons of our estimated instantaneous PAR product (ISCCP-ITP) at
704 spatial resolutions of (a) 10 km, (b) 30 km, and (c) hourly PAR of the CERES
705 SYN1deg (edition 4.1) with observed PAR collected at 42 NEON stations.

706 **Figure 4** Spatial distribution of (a) MBE ($W m^{-2}$) and (b) RMSE ($W m^{-2}$) for our
707 estimated instantaneous PAR product (ISCCP-ITP, 30 km) at seven
708 SURFRAD stations and 42 NEON stations.

709 **Figure 5** Comparisons of our estimated daily PAR product (ISCCP-ITP) at spatial
710 resolutions of (a) 10 km and (b) 30 km with observed PAR collected at seven
711 SURFRAD stations.

712 **Figure 6** Comparisons of our estimated daily PAR product (ISCCP-ITP) at spatial
713 resolutions of (a) 10 km and (b) 30 km with observed PAR collected at 42
714 NEON stations.

715 **Figure 7** Same as **Figure 4**, but for our estimated daily PAR product (ISCCP-ITP, 30
716 km).

717 **Figure 8** Comparisons of our estimated daily PAR product (ISCCP-ITP) at spatial
718 resolutions of (a) 10 km, (b) 30 km, and (c) daily PAR of the CERES



719 SYN1deg (edition 4.1) with observed PAR collected at 38 CERN stations.

720 **Figure 9** Spatial distribution of (a) MBE (W m^{-2}) and (b) RMSE (W m^{-2}) for our

721 estimated daily PAR product (ISCCP-ITP, 30 km) at 38 CERN stations.

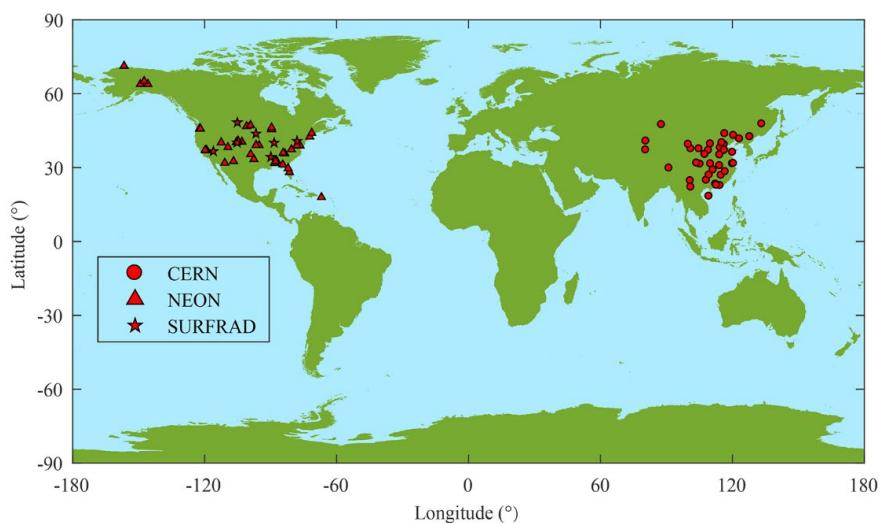
722 **Figure 10** Spatial distribution of annual mean PAR between 2001 and 2018, derived

723 from (a) our estimated PAR product (ISCCP-ITP), and (b) the CERES PAR

724 product. The unit of PAR is W m^{-2} .

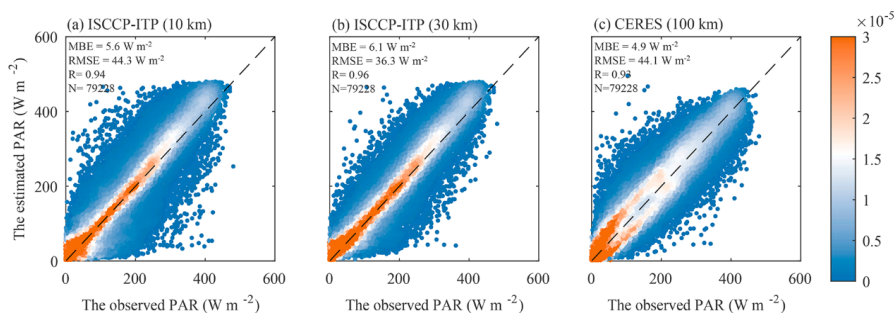
725 **Figure 11** Spatial distribution of seasonal mean PAR between 2001 and 2018 derived

726 from our estimated PAR product (ISCCP-ITP). The unit of PAR is W m^{-2} .



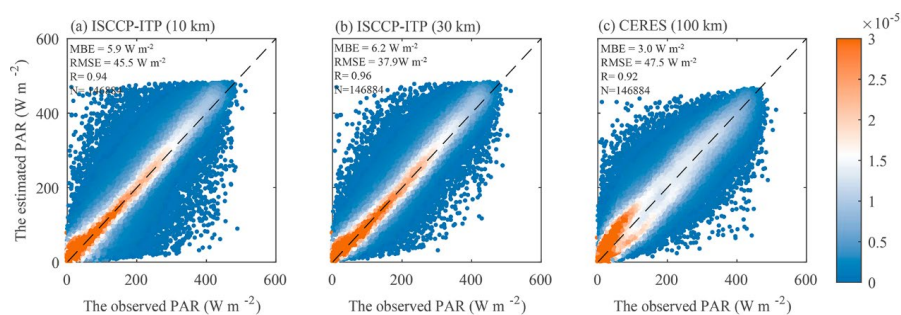
727

728 **Figure 1** Distribution of observation stations within the three observation networks,
729 where measurements of PAR were carried out. The red circles denote the
730 locations of the 38 CERN stations, the red triangles denote the 42 NEON
731 stations, and the red pentagrams denote the seven SURFRAD stations.



732

733 **Figure 2** Comparisons of our estimated instantaneous PAR product (ISCCP-ITP) at
734 spatial resolutions of (a) 10 km, (b) 30 km, and (c) hourly PAR of the CERES
735 SYN1deg (edition 4.1) with observed PAR collected at seven SURFRAD
736 stations.

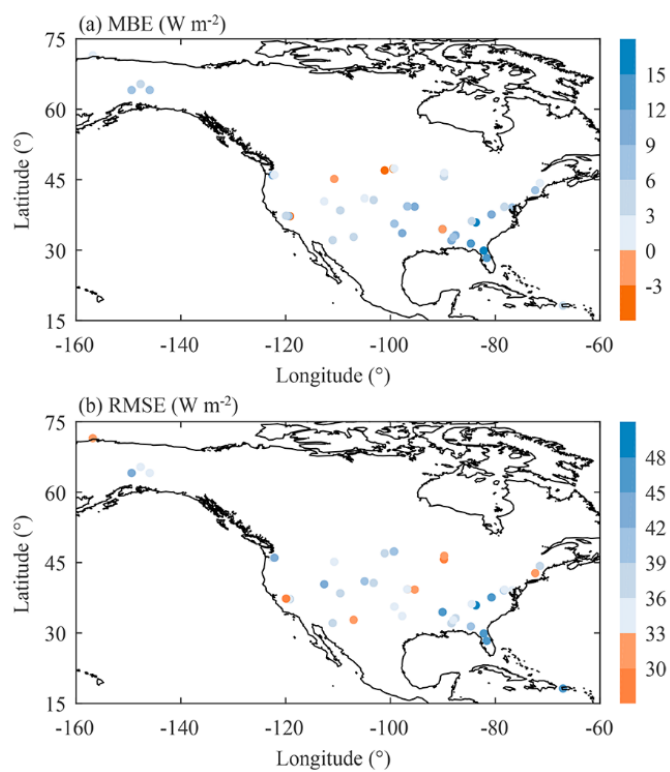


737

738 **Figure 3** Comparisons of our estimated instantaneous PAR product (ISCCP-ITP) at

739 spatial resolutions of (a) 10 km, (b) 30 km, and (c) hourly PAR of the CERES

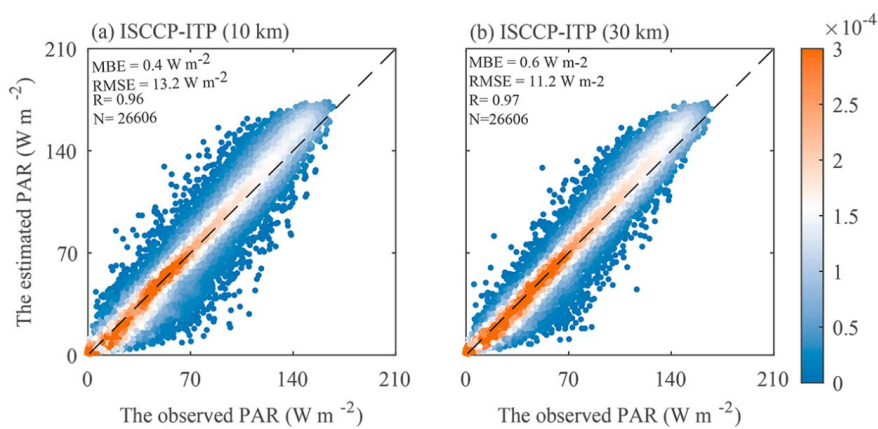
740 SYN1 deg (edition 4.1) with observed PAR collected at 42 NEON stations.



741

742 **Figure 4** Spatial distribution of (a) MBE (W m⁻²) and (b) RMSE (W m⁻²) for our
743 estimated instantaneous PAR product (ISCCP-ITP, 30 km) at seven
744 SURFRAD stations and 42 NEON stations.

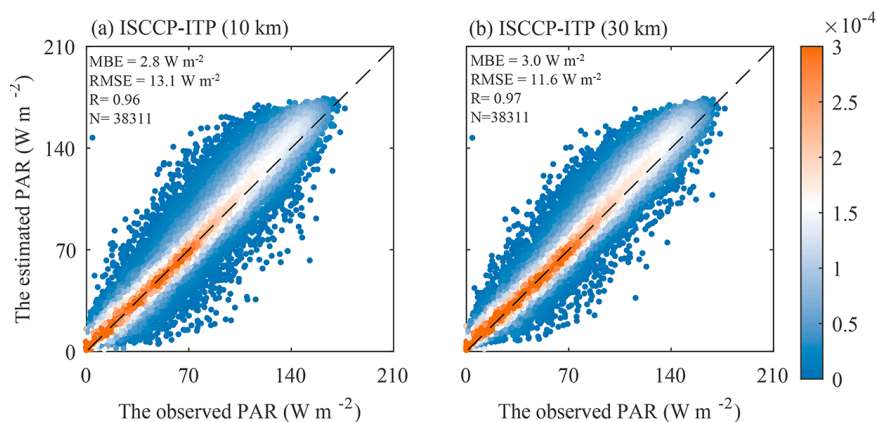
745



746

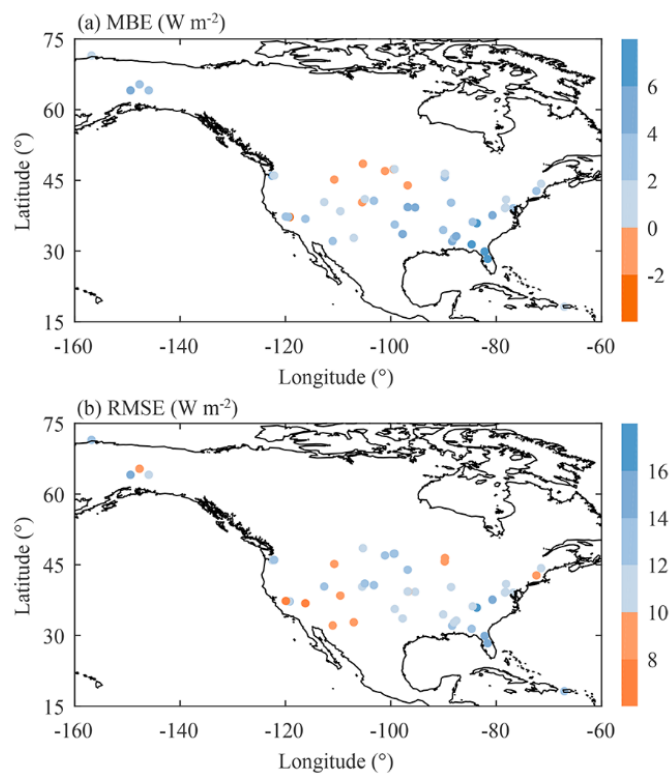
747 **Figure 5** Comparisons of our estimated daily PAR product (ISCCP-ITP) at spatial
748 resolutions of (a) 10 km and (b) 30 km with observed PAR collected at seven
749 SURFRAD stations.

750



751

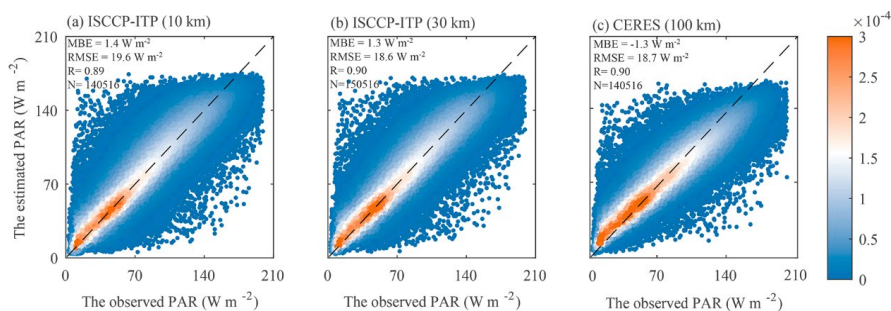
752 **Figure 6** Comparisons of our estimated daily PAR product (ISCCP-ITP) at spatial
753 resolutions of (a) 10 km and (b) 30 km with observed PAR collected at 42
754 NEON stations.



755

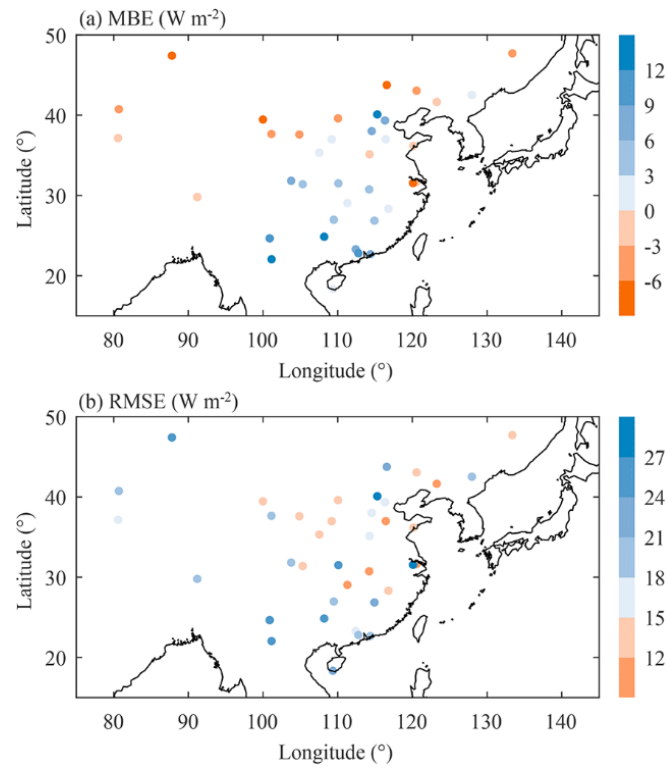
756 **Figure 7** Same as **Figure 4**, but for our estimated daily PAR product (ISCCP-ITP, 30

757 km).



758

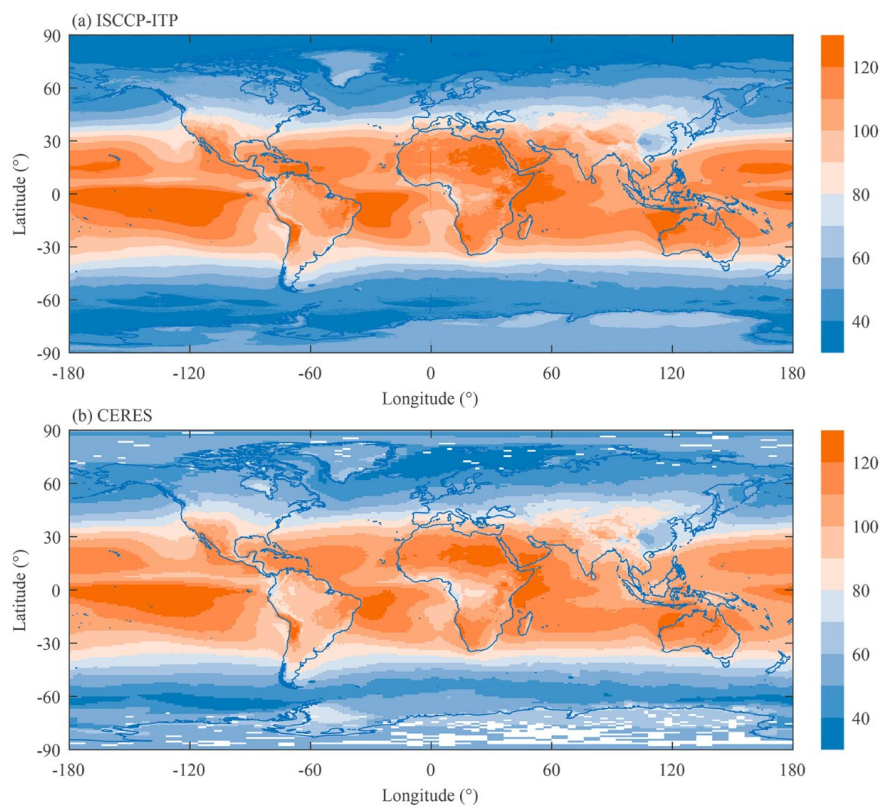
759 **Figure 8** Comparisons of our estimated daily PAR product (ISCCP-ITP) at spatial
760 resolutions of (a) 10 km, (b) 30 km, and (c) daily PAR of the CERES
761 SYN1deg (edition 4.1) with observed PAR collected at 38 CERN stations.



762

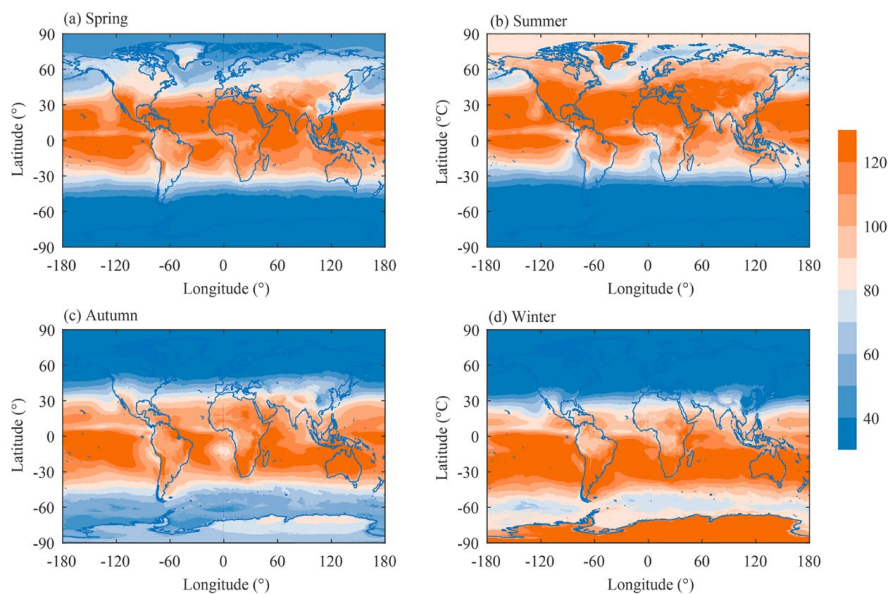
763 **Figure 9** Spatial distribution of (a) MBE (W m^{-2}) and (b) RMSE (W m^{-2}) for our

764 estimated daily PAR product (ISCCP-ITP, 30 km) at 38 CERN stations.



765

766 **Figure 10** Spatial distribution of annual mean PAR between 2001 and 2018, derived
767 from (a) our estimated PAR product (ISCCP-ITP), and (b) the CERES PAR
768 product. The unit of PAR is W m^{-2} .



769

770 **Figure 11** Spatial distribution of seasonal mean PAR between 2001 and 2018 derived
771 from our estimated PAR product (ISCCP-ITP). The unit of PAR is $W m^{-2}$.



772 **Table captions**

773 **Table 1.** Effect of spatial resolution (from 10 km to 110 km) on accuracy of our
774 estimated instantaneous PAR product (ISCCP-ITP) compared to observations
775 at the seven SURFRAD stations.

776 **Table 2.** Effect of spatial resolution (from 10 km to 110 km) on accuracy of our
777 estimated instantaneous PAR product (ISCCP-ITP) compared to observations
778 at the 42 NEON stations.

779 **Table 3.** Effect of spatial resolution (from 10 km to 110 km) on accuracy of our
780 estimated daily PAR product (ISCCP-ITP) compared to observations at the
781 seven SURFRAD stations.

782 **Table 4.** Effect of spatial resolution (from 10 km to 110 km) on accuracy of our
783 estimated daily PAR product (ISCCP-ITP) compared to observations at the
784 42 NEON stations.

785 **Table 5.** Effect of spatial resolution (from 10 km to 110 km) on accuracy of our
786 estimated daily PAR product (ISCCP-ITP) compared to observations at the
787 38 CERN stations.



788 **Table 1.** Effect of spatial resolution (from 10 km to 110 km) on accuracy of our
789 estimated instantaneous PAR product (ISCCP-ITP) compared to observations
790 at the seven SURFRAD stations.

	Spatial resolution	MBE (W m^{-2})	RMSE (W m^{-2})	<i>R</i>
ISCCP-ITP	10 km	5.6	44.3	0.94
ISCCP-ITP	30 km	6.1	36.3	0.96
ISCCP-ITP	50 km	6.0	35.0	0.96
ISCCP-ITP	70 km	5.9	35.1	0.96
ISCCP-ITP	90 km	6.0	35.5	0.96
ISCCP-ITP	110 km	5.9	36.0	0.96

791



792 **Table 2.** Effect of spatial resolution (from 10 km to 110 km) on accuracy of our
793 estimated instantaneous PAR product (ISCCP-ITP) compared to observations
794 at the 42 NEON stations.

	Spatial resolution	MBE (W m^{-2})	RMSE (W m^{-2})	<i>R</i>
ISCCP-ITP	10 km	5.9	45.5	0.94
ISCCP-ITP	30 km	6.2	37.9	0.96
ISCCP-ITP	50 km	6.3	37.0	0.96
ISCCP-ITP	70 km	6.2	37.4	0.96
ISCCP-ITP	90 km	6.2	38.0	0.96
ISCCP-ITP	110 km	6.1	38.6	0.95



795 **Table 3.** Effect of spatial resolution (from 10 km to 110 km) on accuracy of our
796 estimated daily PAR product (ISCCP-ITP) compared to observations at the
797 seven SURFRAD stations.

	Spatial resolution	MBE (W m^{-2})	RMSE (W m^{-2})	<i>R</i>
ISCCP-ITP	10 km	0.4	13.2	0.96
ISCCP-ITP	30 km	0.6	11.2	0.97
ISCCP-ITP	50 km	0.5	10.5	0.98
ISCCP-ITP	70 km	0.5	10.1	0.98
ISCCP-ITP	90 km	0.5	9.9	0.98
ISCCP-ITP	110 km	0.5	9.8	0.98

798

799



800 **Table 4.** Effect of spatial resolution (from 10 km to 110 km) on accuracy of our
801 estimated daily PAR product (ISCCP-ITP) compared to observations at the
802 42 NEON stations.

	Spatial resolution	MBE (W m^{-2})	RMSE (W m^{-2})	<i>R</i>
ISCCP-ITP	10 km	2.8	13.1	0.96
ISCCP-ITP	30 km	3.0	11.6	0.97
ISCCP-ITP	50 km	3.0	11.4	0.97
ISCCP-ITP	70 km	3.0	11.5	0.97
ISCCP-ITP	90 km	3.0	11.7	0.97
ISCCP-ITP	110 km	2.9	11.8	0.97

803



804 **Table 5.** Effect of spatial resolution (from 10 km to 110 km) on accuracy of our
805 estimated daily PAR product (ISCCP-ITP) compared to observations at the
806 38 CERN stations.

	Spatial resolution	MBE (W m^{-2})	RMSE (W m^{-2})	<i>R</i>
ISCCP-ITP	10 km	1.4	19.6	0.89
ISCCP-ITP	30 km	1.3	18.6	0.90
ISCCP-ITP	50 km	1.2	18.3	0.90
ISCCP-ITP	70 km	1.2	18.3	0.90
ISCCP-ITP	90 km	1.1	18.2	0.90
ISCCP-ITP	110 km	1.1	18.3	0.90

807